

Banner appropriate to article type will appear here in typeset article

Deep reinforcement transfer learning for active flow control of a 3D square cylinder under state dimension mismatch

Lei Yan¹, Gang Hu^{1,2,†}, Wenli Chen³, and Bernd R. Noack⁴

¹Artificial Intelligence for Wind Engineering (AIWE) Lab, School of Civil and Environmental Engineering, Harbin Institute of Technology, Shenzhen 518055, China

²Guangdong Provincial Key Laboratory of Intelligent and Resilient Structures for Civil Engineering, Harbin Institute of Technology, Shenzhen, 518055, China

³Key Laboratory of Smart Prevention and Mitigation of Civil Engineering Disasters, the Ministry of Industry and Information Technology, Harbin Institute of Technology, Harbin, 150090, China

⁴School of Mechanical Engineering and Automation, Harbin Institute of Technology, Shenzhen 518055, China

(Received xx; revised xx; accepted xx)

This paper focuses on developing a deep reinforcement learning (DRL) control strategy to mitigate aerodynamic forces acting on a three dimensional (3D) square cylinder under high Reynolds number flow conditions. Four jets situated at the corners of the square cylinder are used as actuators and pressure probes on the cylinder surface are employed as feedback observers. The Soft Actor-Critic (SAC) algorithm is deployed to identify an effective control scheme. Additionally, we pre-train the DRL agent using a two dimensional (2D) square cylinder flow field at a low Reynolds number ($Re = 1000$), followed by transferring it to the 3D square cylinder at $Re = 22000$. To address the issue of state dimension mismatch in transfer learning from 2D to 3D case, a state dimension mismatch transfer learning method is developed to enhance the SAC algorithm, named SDTL-SAC. The results demonstrate transfer learning across different state spaces achieves the same control policy as the SAC algorithm, resulting in a significant improvement in training speed with a training cost reduction of 51.1%. Furthermore, the SAC control strategy leads to a notable 52.3% reduction in drag coefficient, accompanied by substantial suppression of lift fluctuations. These outcomes underscore the potential of DRL in active flow control, laying the groundwork for efficient, robust, and practical implementation of this control technique in practical engineering.

Key words: Authors should not enter keywords on the manuscript, as these must be chosen by the author during the online submission process and will then be added during the typesetting process (see [Keyword PDF](#) for the full list). Other classifications will be added at the same time.

† Email address for correspondence: hugang@hit.edu.cn

1. Introduction

In the fields of fluid dynamics and wind engineering, mitigating the aerodynamic forces acting on a square cylinder under high turbulence flow environment is a pivotal research topic. Under high Reynolds number flow conditions, the wake of the square cylinder exhibits instability, leading to complex vortex shedding. Flow control to mitigate aerodynamic forces of square cylinders is crucial to ensure their aerodynamic stability. In the past, a number of passive and active flow control (AFC) strategies have been developed. Compared to the passive flow control, the AFC strategies are normally more efficient.

Active flow control (AFC) has embraced the continuous integration of advanced machine learning methods, with a notable emphasis on leveraging the deep reinforcement learning (DRL) paradigm rooted in trial-and-error concepts. The DRL paradigm utilizes evaluation data to adapt the control law, aiming to maximize a specified performance metric. The fundamental concept involves promoting actions or policies conducive to the targeted metric. Currently, there is substantial relevant research employing DRL to address issues related to AFC including vortex-induced vibration (Zheng *et al.* 2021; Ren *et al.* 2021; Chen *et al.* 2023), shape optimization (Liu *et al.* 2022; Viquerat *et al.* 2021; Li *et al.* 2021), optimization of the movement collective fish (Gazzola *et al.* 2016), and turbulent flow control (Guastoni *et al.* 2023; Ren *et al.* 2019; Yan *et al.* 2023). The application of DRL for reducing the drag of the cylinder was first introduced by Rabault *et al.* (2019), resulting in a notable stable drag reduction of approximately 8% at $Re = 100$. Meanwhile, Tang *et al.* (2020) implemented four synthetic jets symmetrically positioned on the lower and upper sides of a cylinder to control the flow, as well as demonstrated that DRL can effectively discern various control strategies across different Re . Han *et al.* (2022) minimized the mean drag coefficient of a cylinder by optimizing the angular velocity of a rotating circle. Previous studies have convincingly demonstrated the efficacy of DRL in acquiring control policies for complex environments, particularly those characterized by high dimensionality and nonlinearity (Vignon *et al.* 2023).

Despite the crucial role played by DRL algorithms in understanding and improving the behavior of 2D flow control (Paris *et al.* 2021, 2023), there are inherent limitations in 2D flow control when simulating the intricate 3D characteristics of real flow fields. In practice, flow field control often involves interactions across multiple dimensions, and 2D models frequently fail to accurately capture the essence of these interactions. Consequently, to achieve a more comprehensive understanding and mastery of flow behavior, researchers have progressively shifted their focus from 2D flow control to the more intricate realm of 3D flow control (Suárez *et al.* 2023). However, within the framework of 3D flow control, challenges persist due to the dynamic complexity and non-linear nature of flow fields, leading to difficulties such as time consuming training of control policy. For instance, in the investigation by Fan *et al.* (2020), a month is required to train the DRL control strategy with $Re = 10^4$. As Re escalates to higher levels, the time cost associated with direct DRL training becomes unacceptable.

To address these challenges, the introduction of transfer learning has emerged as a viable approach. transfer learning facilitates the acceleration of the learning process for models in target tasks by sharing knowledge across various tasks or domains. This practice enhances the accuracy of modeling and control for complex flow fields. He *et al.* (2023) introduces a policy transfer strategy utilizing DRL, demonstrating drag reduction in both 2D and 3D flow environments, with increased effectiveness at higher Re in the 3D environment. While learning from simulated data is uninhibited, the speed of simulation imposes limitations. Moreover, subsequent work by Wang *et al.* (2023b) showcases the application of transfer learning to expedite DRL in controlling cylinder flows at high Re , achieving enhanced stability and reduced training episodes, with a specific focus on wake flow at $Re = 1.4 \times 10^5$. This implies the feasibility of transferring knowledge from low Re to high Re .

The majority of the aforementioned studies primarily rely on direct transfer learning under state dimension consistency for acceleration. However, there is a notable absence of a cross-domain transfer learning algorithm applicable to 3D flow control. One possible reason is that transferring a control strategy from a 2D flow field to a 3D flow field environment presents a significant challenge due to changes in the state space. Conventional transfer learning methods struggle to address the inconsistency induced by this state-space shift, impeding DRL agents from effectively learning knowledge from diverse state-space flow field policy. Acknowledging this challenge, the state dimension mismatch transfer learning coupled with the SAC algorithm (SDTL-SAC) is proposed in this study. In the 3D flow around a square cylinder, this method substantially enhances the convergence performance of the DRL algorithm by facilitating cross-domain transfer learning through an encoder and extracting control policy from 2D flow fields.

This study initiates by presenting the control performance within the 3D flow field of a square cylinder employing a multiple jet configuration scheme. A cross-domain transfer learning method is used to transfer the domain knowledge from the 2D square cylinder flow field to the 3D square cylinder flow field under the mismatch in state dimensions. The rest of the paper is organized as follows: Section 2 provides details of the simulation model and the numerical method of the 2D and 3D square cylinder. Section 3 outlines the DRL methodology underlying the algorithm and introduces the SDTL-SAC. The performance of the DRL control on a square cylinder under $Re = 22000$ and the results of the transfer learning method are discussed in Section 4. Finally, Section 5 gives the conclusion of the paper and the limitations of the proposed transfer algorithm are discussed.

2. Description of the flow configuration and numerical methods

This section begins with a numerical simulation configuration of a 2D square cylinder in Section 2.1. Section 2.2 provides a comprehensive introduction to the numerical simulation configuration of a 3D square cylinder. The accuracy of these numerical algorithms is then scrutinized for validation purposes. Finally, the flow control configuration scheme is introduced in Section 2.3, incorporating the placement of four jets at the corners of the square cylinder as actuators for AFC. The goal is to mitigate the drag force and lift fluctuation of the square cylinder.

2.1. Numerical simulation configuration of 2D square cylinder

The open-source computational fluid dynamics package OpenFOAM (Jasak *et al.* 2007) is used in the simulations in this study. The flow is considered as viscous and incompressible. The governing equations are the two-dimensional Navier-Stokes equation and a non-dimensional continuity equation can be expressed as follows:

$$\frac{\partial \mathbf{u}}{\partial t} + \mathbf{u} \cdot (\nabla \mathbf{u}) = -\nabla p + Re^{-1} \Delta \mathbf{u}, \quad (2.1)$$

$$\nabla \cdot \mathbf{u} = 0, \quad (2.2)$$

where \mathbf{u} , t and p are the non-dimensional velocity, time, and pressure respectively, the characteristic length is the length of the square cylinder D , ν is the kinematic viscosity of the fluid and $\bar{U} = 2m/s$ is the mean velocity at the inlet. The Reynolds number is defined as $Re = \bar{U}D/\nu = 1000$.

The computational domain for the square cylinder is depicted in Fig. 1. The inlet boundary (Γ_{in}) is characterized by a uniform velocity inlet boundary condition. Additionally, the outlet boundary (Γ_{out}) is specified as a pressure outlet, maintaining zero velocity gradient and

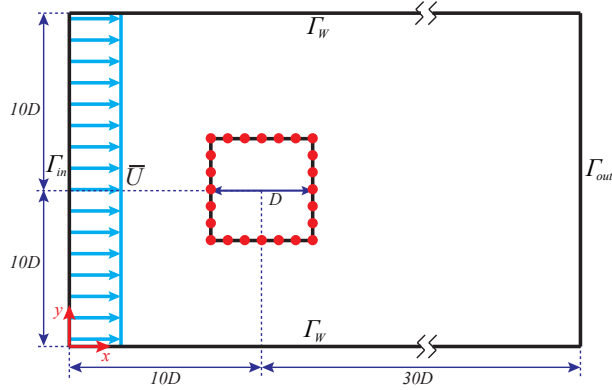


Figure 1: Description of 2D square cylinder numerical setup: the origin of the coordinates is located at the center of the square cylinder. Γ_{in} stands the inflow velocity with a uniform flow profile, while Γ_{out} is put for the outflow. Non-slip wall boundary constraint Γ_w is applied on the bottom and top of the channel, as well as on the surface of the square cylinder. The red dots represent the positions of the 24 pressure probes.

a constant pressure. The no-slip constraint (Γ_w) is enforced on both the top and bottom surfaces of the domain and on the surface of the 2D square cylinder. The origin of the flow field coordinate system is established at the center of the square cylinder, which has a side width of D . The distance from the inlet to the center of the square cylinder is $10D$, while the outlet boundary is positioned at a distance of $30D$ from the center, ensuring the full development of the wake.

Drawing inspiration from Wang *et al.* (2023a), we position probes strategically on the surface of the square cylinder. The objective of this placement is to gather pressure information from 24 designated probes on the surface used in the subsequent DRL training process. The accuracy of the grid has been validated as demonstrated in the work of Yan *et al.* (2023).

2.2. Numerical simulation configuration of 3D square cylinder

The computational domain dimensions are adapted following the investigation by Trias *et al.* (2015). Distances from the inlet (upstream) and outlet (downstream) to the surface of the square cylinder are set to $9.5D$ and $19.5D$, respectively. Additionally, the distances from the top and bottom surfaces to the surface of the square cylinder are $9.5D$. The span of the square cylinders is πD , as depicted in Fig. 2. The red points on the surface of the square cylinder represent pressure probes arranged in five circles, each containing 24 probes, ensuring comprehensive information about the flow field, as shown in Fig. 2. Besides, $\bar{U} = 6.5\text{m/s}$ is the mean velocity at the inlet Γ_{in} and $Re = 22000$.

The flow simulation employs the large eddy simulation (LES) technique (Yang 2015), solving the 3D Navier-Stokes equations through the finite volume method. The pisoFoam solver, a transient solver for incompressible turbulence using the PISO algorithm (Barton 1998) is selected. Discrete time and spatial derivatives utilize the Crank-Nicolson scheme and the second-order central difference scheme, respectively. A wall-adapted local eddy viscosity model (Nicoud & Ducros 1999) is employed for simulating subgrid-scale stresses. The surface of the square cylinder is subject to a no-slip boundary condition (Γ_w), ensuring fluid adherence. Free slip conditions are applied to the sides and top of the computational domain. At the inlet boundary (Γ_{in}), a uniform free-flow velocity \bar{U} is prescribed. The stress vector at the outlet boundary of the computational domain (Γ_{out}) is set to zero. Other

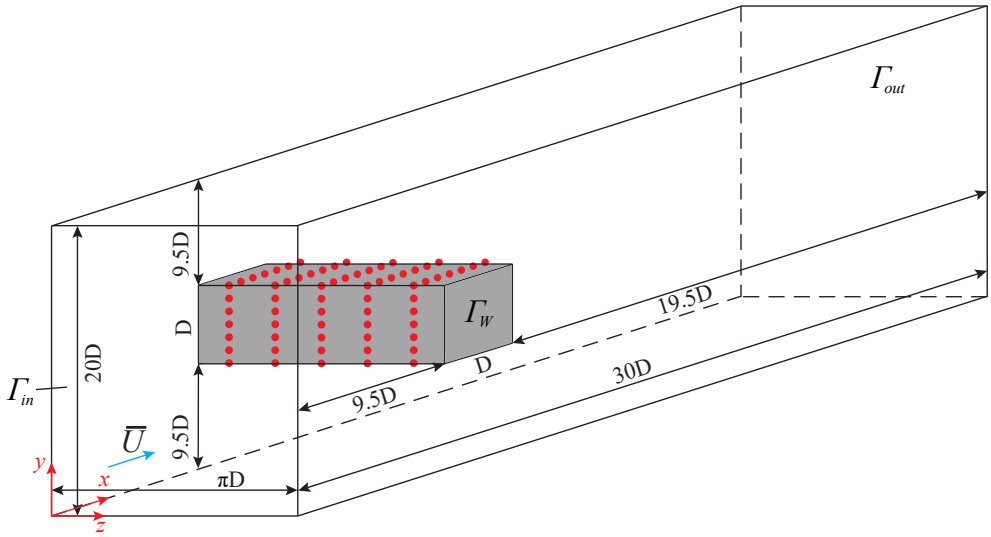


Figure 2: Schematics of the computational domain for 3D turbulent flow around the square cylinder. The red points represent the locations of 120 surface pressure probes.

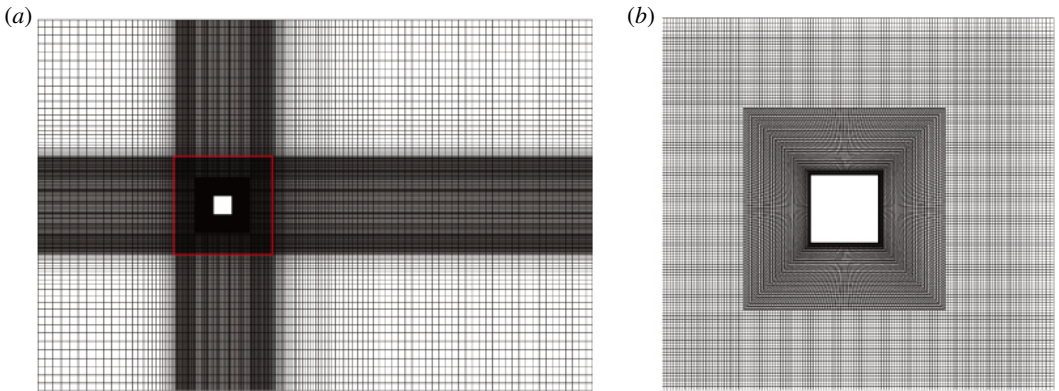


Figure 3: Baseline grids used in the simulation: the full (a) and partial (b) computational domain.

boundaries enforce zero values for the normal component of velocity and the tangential component of the stress vector in both directions. Throughout the time marching solution process, the position, velocity, and boundary conditions of the square cylinder are updated at each nonlinear iteration to accurately capture evolving flow dynamics.

This investigation explores turbulence surrounding a 3D square cylinder at $Re = 22000$. The computational domain is discretized using structured grids of varying sizes, illustrated in Fig. 3. The grid is directly generated from the 3D simulation region to faithfully simulate physical phenomena and minimize numerical diffusion. Special attention is given to mesh refinement around the surface of the square cylinder and jets to enhance simulation accuracy. The study focuses on determining two non-dimensional aerodynamic coefficients: the drag coefficient (C_D) and lift coefficient (C_L):

Table 1: Comparison of integral flow quantities in the flow past a 3D square cylinder at $Re = 22000$. $St = fD/\bar{U}$ is the Strouhal number. LES^i corresponds to each mesh resolution. Reference simulation results from literatures: DNS result(Trias *et al.* 2015); LES results(Rodi *et al.* 1997; Voke 1997);RANS results(Rodi *et al.* 1997; Voke 1997).

	Mesh size	Mean C_D	std of C_D	std of C_L	S_t
Present LES^1	1.4 million	2.15	0.215	1.3	0.125
Present LES^2	2.8 million	2.19	0.218	1.35	0.126
Present LES^3	5.2 million	2.22	0.223	1.42	0.13
DNS result	-	2.18	0.205	1.71	0.132
LES results	-	2.02-2.77	0.14-0.27	1.15-1.79	0.09-0.15
RANS results	-	1.64-2.43	< 0.27	0.31-1.49	0.134-0.159

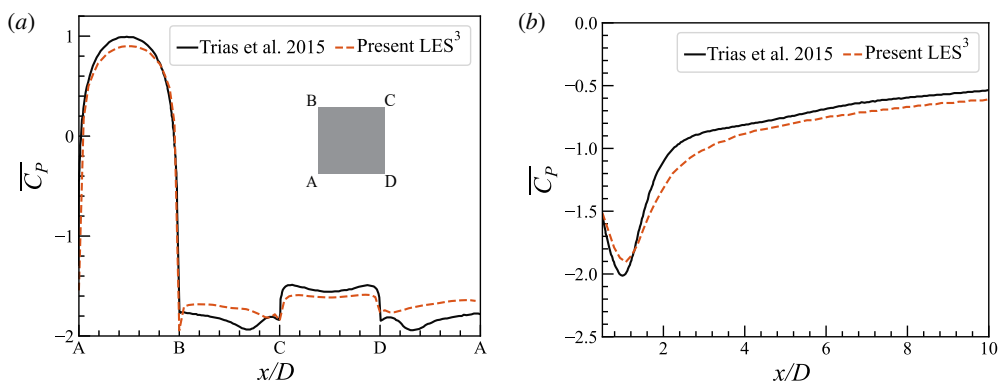


Figure 4: Comparison of mean pressure coefficient C_P correspond to LES^3 result with DNS result of Trias *et al.* (2015) corresponding to (a) around the square cylinder and (b) at domain centerline, respectively.

$$C_D = \frac{2F_x}{\rho\bar{U}^2 DH}, \quad C_L = \frac{2F_y}{\rho\bar{U}^2 DH}, \quad (2.3)$$

where ρ is the density of the fluid in the flow field and $H = \pi D$ denotes the length of the square cylinder. F_x and F_y denote the aerodynamic forces acting in the downwind (x direction in Fig. 2) and crosswind (y direction in Fig. 2) directions on the square cylinder, respectively. To validate the accuracy of the grid, a grid verified study is conducted. Results from three distinct grid designs are compared with data from various simulations, and the grid convergence outcomes are summarized in Table 1. The statistical values of C_D , C_L , and S_t derived from the simulation at $Re = 22000$ are presented. All three grids employ computational cells of the same size around the square cylinders, differing only in cell size in the wake region. It is noteworthy that the simulation results exhibit robustness to grid resolution, aligning with values obtained from existing literature (Trias *et al.* 2015; Rodi *et al.* 1997; Voke 1997).

For three mesh configurations, mean y^+ for the baseline mesh consistently remains below 1, aligning with the recommendation of Saeedi & Wang (2016). Throughout the simulation, the maximum Courant–Friedrichs–Lewy (CFL) number stays below 1, ensuring the temporal resolution of the unsteady flow. Fig. 4 presents a comparison of the mean values of the pressure

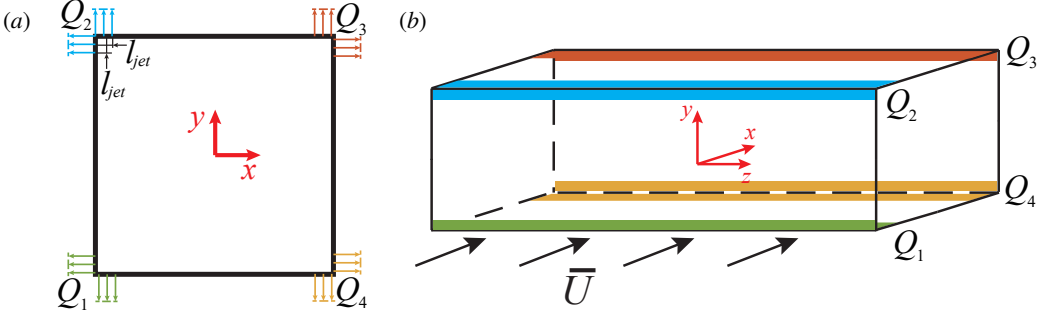


Figure 5: Details of four jet location and control configuration scheme in the (a) 2D and (b) 3D flow field of the square cylinder. The shaped regions on each corner side of the square cylinder represent the jet actuators Q_1 , Q_2 , Q_3 , and Q_4 . l_{jet} represents the length of the jet actuator.

coefficient (C_P) distribution around the square cylinder and in the wake flow, contrasting the results with a DNS simulation study (Trias *et al.* 2015). Notably, the numerical outcomes from Present LES³ exhibit a favorable agreement with the DNS simulations concerning mean values, with minimal disparities in the surface and wake region of the square cylinder. This underscores the reliability of the simulations. Given the considerable time required for coarse grid simulations, the grid configuration of Present LES¹ is employed in the subsequent DRL training, while Present LES³ is utilized for testing to optimize computational efficiency.

2.3. Configurations of flow control for the square cylinder

Considering the intricate and highly turbulent flow field around the square cylinder, the independence of each jet is set when implementing AFC. Illustrated in Fig. 5, four jet actuators Q_1 , Q_2 , Q_3 , and Q_4 are strategically positioned at four corners of the square cylinder. Irrespective of the control mode (blowing or suction), the velocities of the four jets are consistently directed perpendicular to the surface of the square cylinder. Moreover, the DRL agent is deployed to generate four distinct actions for controlling each jet. This ensures that the velocity value at any corner of the square cylinder remains constant, aligning with the control objectives.

Based on uniformity in jet actuator control, the length of each jet consistently is maintained at $1/25$ of the corresponding side length. Regardless of the wind attack angle, the ratio l_{jet}/D remains a constant of $1/25$. The mass flow rate Q_i^* for each Q_i is defined as:

$$Q_i^* = Q_i/Q_{ref} = \frac{U_{jet,i} \cdot 2l_{jet}}{U \cdot D} \quad (2.4)$$

where Q_i is the blowing and suction flow rate corresponding to Fig. 5 and $U_{jet,i}$ is i_{th} jet velocity. Q_i^* is not greater than 0.037 in this study.

To prevent non-physical abrupt alterations in pressure and velocity caused by jet actuator control, a continuous time approach is employed for the control mechanism in the CFD algorithms. Additionally, the proper choice of an interpolation method is pivotal for serializing the received time-discretized control signal in this system. Consequently, the jet actuation undergoes smoothing to guarantee a continuous transition in the control signal, preventing excessive lift fluctuations arising from sudden changes in jet velocity. The alteration process in jet velocity between each action step is linearly defined (Yan *et al.* 2023).

$$V_{\Gamma_i(t)} = V_{\Gamma_i(t-1)} + [a - a_{(t-1)}]/N_e, \quad i = 1, 2, \quad (2.5)$$

where $V_{\Gamma_i(t)}$ is the jet flow velocity used at the non-dimensional times t , and a is the jet velocity of Γ_i for the current action time step.

3. Reinforcement learning algorithms

In this section, the basic Soft Actor-Critic (SAC) algorithm (Haarnoja *et al.* 2018) is first introduced. Then, how to learn state embeddings and how to adaptively transfer one cross-domain source policy to learn the current policy is described. Finally, the state dimension mismatch transfer learning method (SDTL) combined with the basic SAC algorithm is illuminated in detail.

3.1. Description of off-policy reinforcement learning

In this study, DRL within the context of an infinite-horizon discrete-time Markov Decision Process (MDP) which denoted as $\mathcal{M} = \langle \mathcal{S}, \mathcal{A}, \mathcal{R}, \mathcal{T}, \gamma \rangle$, where \mathcal{S} and \mathcal{A} represent the sets of states and actions, respectively. The state transition probability function is denoted as $\mathcal{T} : \mathcal{S} \times \mathcal{A} \times \mathcal{S} \mapsto [0, 1]$, and the reward function, evaluating agent performance, is denoted as $\mathcal{R} : \mathcal{S} \times \mathcal{A} \times \mathcal{S} \mapsto \mathbb{R}$. The discount factor for future rewards is represented by γ . A policy $\pi : \mathcal{S} \times \mathcal{A} \mapsto [0, 1]$ is defined as a state-conditioned probability distribution over actions, and the agent objective is to discover an optimal policy π^* that maximizes the expected discounted return $R = \sum_{i=t}^T \gamma^{i-t} r_i$.

The deep deterministic policy gradient (DDPG) off-policy algorithm (Lillicrap *et al.* 2015) is extensively employed for estimating the gradient of the DRL objective. Soft Actor-Critic (SAC) (Haarnoja *et al.* 2018) is one of the most efficient off-policy algorithms and is designed for proficiently learning randomized policies and facilitating maximum entropy reinforcement learning. Entropy serves as a quantification of the randomness inherent in a random variable. Specifically, for a random variable X with a probability density function denoted as p , its entropy H is defined as $H(X) = \mathbb{E}_{x \sim p} [-\log p(x)]$. In the context of reinforcement learning, $H(\pi(\cdot|s))$ characterizes the extent of randomness in a policy within a given state.

The concept behind maximum entropy reinforcement learning involves not only maximizing cumulative rewards but also making the control strategy that exhibits increased randomness. To achieve this, an entropy regularization term is incorporated into the DRL objective, defined as:

$$\pi^* = \arg \max_{\pi} \mathbb{E}_{\pi} \left[\sum_t r(s_t, a_t) + \alpha H(\pi(\cdot|s_t)) \right] \quad (3.1)$$

where α is a regularization factor to control the importance of entropy. Entropy regularization plays a pivotal role in enhancing the exploration aspect of the DRL algorithm. A higher value for α amplifies the exploratory nature, expediting subsequent policy learning and mitigating the risk of the policy converging to a suboptimal local minimum.

Within the framework of Maximum Entropy Reinforcement Learning, the Soft Bellman equation is expressed as follows:

$$Q(s_t, a_t) = r(s_t, a_t) + \gamma \mathbb{E}_{s_{t+1}} [V(s_{t+1})] \quad (3.2)$$

where the state value function is written as

$$V(s_t) = \mathbb{E}_{a_t \sim \pi} [Q(s_t, a_t) - \alpha \log \pi(a_t|s_t)] \quad (3.3)$$

The SAC algorithm incorporates two value functions Q parameterized by ψ_1 and ψ_2 respectively, along with a policy function π parameterized by θ , as illustrated in Fig. 6.

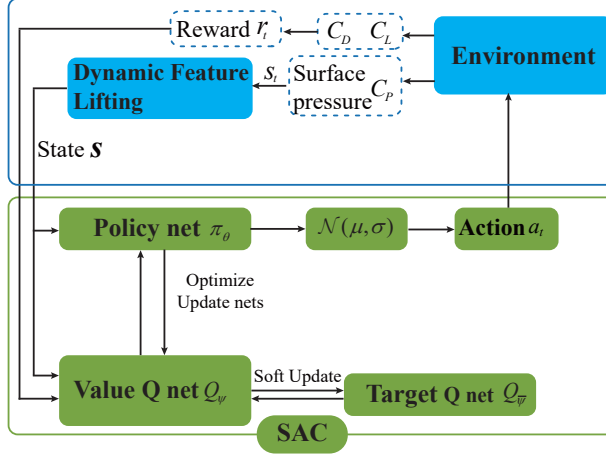


Figure 6: Schematic of SAC algorithm framework used in the present study. The Q network update: the target Q net Q_{ψ}^- gets the target Q value based on \mathbf{s} , then the value Q net Q_{ψ} gets the desired Q value. The policy net π_{θ} update: Use the value Q net updated to calculate the desired value based on \mathbf{s} and r_t . Then calculate the loss for the network parameter update and outputs μ and σ , which are used to sample action a_t . Noteworthy, the Dynamic Feature Lifting method is used from Wang *et al.* (2023a) in order to develop an effective flow state estimation that enables the DRL agent can obtain efficient information based on it. This framework is derived from the DRLinFluids package (Wang *et al.* 2022).

Drawing inspiration from the concept of DDPG, the SAC employs two distinct networks for Q function. Notably, each time a Q network is utilized, it selects the network associated with a smaller Q value. This approach mitigates the issue of value overestimation. The loss function for each value function is expressed as follows:

$$L_Q(\psi) = \mathbb{E}_{(s_t, a_t, r_t, s_{t+1}) \sim \mathcal{D}} \left[\frac{1}{2} \left(Q_{\psi}(s_t, a_t) - (r_t + \gamma V_{\psi}^-(s_{t+1})) \right)^2 \right] \quad (3.4)$$

where \mathcal{D} is the data collected in the historical training process since SAC is an off-policy algorithm. To enhance training stability, the present networks Q_{ψ}^- are employed. Specifically, two current networks Q are utilized sequentially, aligning with the two corresponding Q networks. The updating procedure for the current networks in SAC mirrors that of DDPG. The loss function for the strategy function π is derived from the Kullback-Leibler (KL) divergence and is subsequently simplified to:

$$L_{\pi}(\theta) = \mathbb{E}_{s_t \sim \mathcal{D}, a_t \sim \pi_{\theta}} [\alpha \log(\pi_{\theta}(a_t | s_t)) - Q_{\psi}(s_t, a_t)] \quad (3.5)$$

In addition, as illustrated in Fig. 6, the SAC algorithm proceeds through each step by selecting four actions a_t based on the current policy, executing these actions, and observing the resulting environmental feedback, including rewards r_{t+1} and the subsequent state S_{t+1} . The state S_{t+1} is then constructed as a state representation (S), incorporating historical time series data through the application of the Dynamic Feature Lifting method (Wang *et al.* 2023a). This involves leveraging pressure data from surface probes on the square cylinder collected over the preceding 30 action time steps. Notably, the performance of the DRL agent is significantly enhanced by transforming sensor signals into dynamic features. Consequently, the agent can effectively utilize surface pressure data instead of relying on velocity information from the wake.

3.2. Learning state correspondence

In this section, the aim is to distill knowledge from a pre-trained source policy to a current policy with the aim of enhancing the sample efficiency of the ongoing learning process, which is presented from Wan *et al.* (2020). The problem is set as considering scenarios where the source and current policies operate within distinct MDPs. The MDP properties $(\mathcal{S}, \mathcal{A}, \mathcal{R}, \mathcal{T}, \gamma)$ could be different, but a fundamental structural commonality persists between source and current MDPs. This commonality exemplified by the transfer from a 2D flow fluid to a 3D flow fluid (He *et al.* 2023), allows for the adaptation of knowledge. For notational simplicity, $\mathcal{S}_{\text{source}}$ and $\mathcal{S}_{\text{current}}$ denote the state spaces of the source and current MDPs, respectively. Here assume the availability of a pre-trained source policy network within the source MDP and concentrate on extracting representations from this source policy network that prove beneficial for learning within the current MDP. Moreover, the challenge of knowledge transfer is arised when $\mathcal{S}_{\text{source}} \neq \mathcal{S}_{\text{current}}$. To address this mismatch, a learned embedding space parameterized by an encoder function $\phi(\cdot)$ which is defined as $\mathcal{S}_{\text{emb}} := \{\phi(s) \mid s \in \mathcal{S}_{\text{current}}, \phi(s) \in \mathcal{S}_{\text{source}}\}$. Data points from this embedding space serve to extract valuable information from the source policy network. To ensure compatibility, the dimension of the embedding space is enforced to match the state space in the source MDP ($|\mathcal{S}_{\text{emb}}| = |\mathcal{S}_{\text{source}}|$). It is worth noting that any embedding vector $s \in \mathcal{S}_{\text{emb}}$ is not necessarily a valid input state in the source MDP.

Hence, the encoder parameter (ϕ) plays a pivotal role in ensuring that the generated embeddings align with the DRL objective. In order to transfer from a source pre-trained policy to a current policy within the current MDP in disparate state spaces, lateral connections are incorporated between the current and source networks which can enhance representations in the layers of the current network by incorporating valuable representations from the layers of the source network. Consequently, this facilitates the extraction of transferable knowledge from both the source policy and state-value networks. Additionally, the source policy and value network are represented by π'_{θ} and V'_{ψ} , respectively, where the parameters (θ', ψ') remain fixed throughout training. In parallel, (θ, ψ) denote the trainable parameters for the current policy and value networks. As a general assumption for simplicity of exposition, the source and current policy and value networks are presumed to share the same number of hidden layers (N_{π} and N_Q).

In the current MDP, the current policy observes a state $s_{\text{current}} \in \mathcal{S}_{\text{current}}$ and then fed it into the encoder to produce state embedding $\phi(s_{\text{current}}) \in \mathcal{S}_{\text{emb}}$, which can be easily passed through the source networks to extract $\{z_{\theta'}^i, z_{\psi'}^i, 1 \leq i \leq N_{\pi}, 1 \leq i \leq N_Q\}$ representing the pre-activation outputs of the i -th hidden layers of the source policy and value networks. Consequently, to acquire the hidden layer outputs $\{z_{\pi_{\theta}}^i, z_{Q_{\psi}}^i\}$ at layer i in the current networks, the following relationships hold:

$$\begin{aligned} z_{\pi_{\theta}}^i &= \sigma(p_{\theta}^i z_{\theta'}^i + (1 - p_{\theta}^i) z_{\theta'}^i), \\ z_{Q_{\psi}}^i &= \sigma(p_{\psi}^i z_{\psi'}^i + (1 - p_{\psi}^i) z_{\psi'}^i) \end{aligned} \quad (3.6)$$

where σ is the activation function. The learnable mixing weights $\{p_{\theta}^i, p_{\psi}^i\} \in [0, 1]$ serve as dynamic factors that evolve over time, governing the diminishing influence of source policy on the current policy – a higher value of $\{p_{\theta}^i, p_{\psi}^i\}$ signifies a reduced impact. These coefficients are initially set to low values during the early stages of training to facilitate the provision of essential information for starting the learning process. However, at the end of the training process, the current policy becomes entirely independent of the source policy,

facilitating swift deployment during test time. To foster this independence, the additional coupling loss terms are designed to drive $\{p_\theta^i, p_\psi^i\}$ towards 1 as the training progresses:

$$L_{\text{coupling}}^\pi = -\frac{1}{N_\pi} \sum_{i=1}^{N_\pi} \log(p_\theta^i), L_{\text{coupling}}^Q = -\frac{1}{N_Q} \sum_{i=1}^{N_Q} \log(p_\psi^i) \quad (3.7)$$

In order to drive the update of encoder parameters (ϕ), it is imperative for the input states and state embeddings to demonstrate a highly correlated, thereby enabling optimal guidance from the source policy. So maximizing the mutual information between states and embeddings is the crucial approach. This objective is articulated as follows, drawing inspiration from (Wan *et al.* 2020):

$$\begin{aligned} \mathcal{I}(s; e) &= \mathcal{H}(s) - \mathcal{H}(s|\phi(s)) \\ &= \mathcal{H}(s) + \mathbb{E}_{s,e} [\log p(s|e)] \\ &= \mathcal{H}(s) + \mathbb{E}_{s,e} [\log q_\omega(s|e)] \\ &\quad + \mathbb{E}_e [D_{\text{KL}}(p(s|e)||q_\omega(s|e))] \\ &\geq \mathcal{H}(s) + \mathbb{E}_{s,e} [\log q_\omega(s|e)] \end{aligned} \quad (3.8)$$

where \mathcal{H} denotes the differential entropy. The optimization objective outlined above is recognized as a variational information maximization algorithm, where the variational distribution $q_\psi(s|e)$ serves as an approximation to the true conditional distribution $p(s|e)$. Consequently, the ultimate optimization objective can be expressed as:

$$\begin{aligned} L_{\text{MI}}^\pi(\phi, \omega) &= -\mathbb{E}_{s \sim \rho_{\pi_\theta}} [\log q_\omega(s_{\text{current}}|\phi(s_{\text{current}}))] \\ L_{\text{MI}}^Q(\phi, \omega) &= -\mathbb{E}_{s \sim \rho_{Q_\psi}} [\log q_\omega(s_{\text{current}}|\phi(s_{\text{current}}))] \end{aligned} \quad (3.9)$$

where ρ_{π_θ} and ρ_{Q_ψ} is the state distribution of the current policy and value network.

3.3. SDTL-SAC algorithm

Fig. 7 illustrates the schematic diagram encompassing the comprehensive architecture and gradient flows, accompanied by a description of the implemented neural networks. This algorithm combines with Mutual Information based Knowledge transfer (Wan *et al.* 2020; You *et al.* 2022) and basic SAC algorithm, specifically addresses state dimensional mismatch problems, named SDTL-SAC. In each iteration, the policy is executed within the current MDP, generating a batch of trajectories. This experience is then utilized to compute both the DRL loss (Equation 3.4 and 3.5) and the mutual information loss (Equation 3.9). The resulting gradients are employed to update various parameters. Simultaneously using these losses to update the encoder (ϕ) ensures the fulfillment of the target for embeddings correlating them with the states in the current MDP. The coupling parameters p_π and p_ψ , essential for the weighted combination of representations in the source and current networks, are updated using the coupling loss (Equation 3.7) in conjunction with the DRL loss. The details of the SDTL-SAC algorithm are described in Appendix B.

To illustrate the viability of employing cross-domain transfer learning in DRL for AFC, two distinct steps are undertaken as follows: first, the basic SAC algorithm is employed to train a control policy aimed at minimizing both C_D and C_L ; second, the SDTL-SAC algorithm is leverage for transfer learning, facilitating the transfer of control policy from a 2D square cylinder flow field to a 3D square cylinder flow field environment for the given application.

The study aims to reduce C_D and C_L of square cylinders by using DRL control. This objective can be achieved by setting an appropriate reward function. The reward function

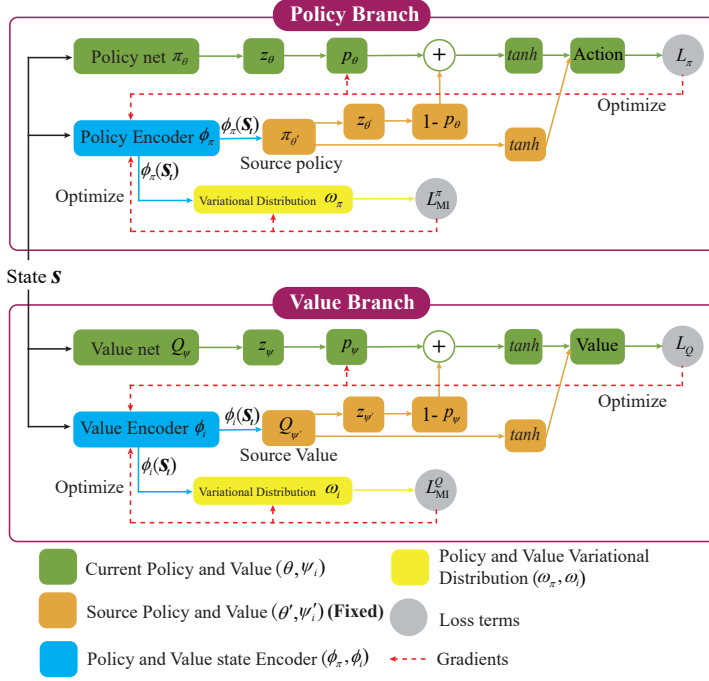


Figure 7: Schematic of the SDTL-SAC framework used in the present study. Within the current networks (green), pre-activation representations are blended linearly, utilizing learned mixing weights, with corresponding representations from the source policy, as detailed in Equations 3.6. The source networks (orange) remain constant throughout training without undergoing gradient updates. The encoder parameters, denoted as ϕ_π (ϕ_v) which depicted in blue, receive gradients from two distinct sources: the policy-gradient loss L_π (or the value function loss L_Q) and the mutual information loss L_{MI}^π (L_{MI}^Q). It is important to note that this knowledge flow occurs across all network layers.

that combines C_D and C_L is proposed to achieve the optimization goal as follows:

$$r_t = -\langle C_D^t \rangle_T - |\langle C_L^t \rangle_T|, \quad (3.10)$$

where C_D^t and C_L^t means instantaneous C_D and C_L at time t respectively, and $\langle \cdot \rangle_T$ indicates the mean value in one action period T with DRL control.

4. Results and discussion

The control performance and reliability of the basic SAC algorithm and a comparative analysis of the flow fields under baseline conditions and SAC control are shown in this section. Additionally, the process of transferring control policies when confronted with a state dimension mismatch from a 2D square cylinder to a 3D square cylinder is elucidated in Section 4.2. Moreover, an investigation into the disparity in DRL training speed between SDTL-SAC and the basic SAC algorithm is conducted.

4.1. Flow control results using the basic SAC algorithm

Following extensive DRL training epochs, the converged policy is convergence by employing four jet control configurations. To comprehensively assess the control efficacy and robustness of the agent, a total of 200 interactions are conducted between the agent and the environment

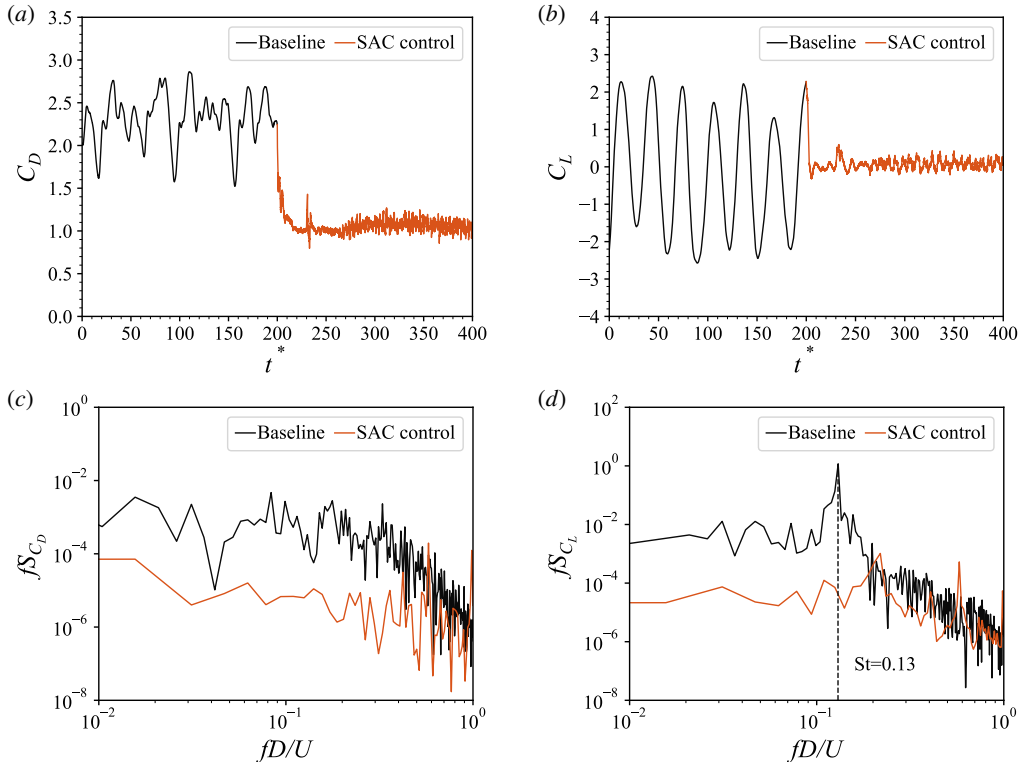


Figure 8: (a) Evolution of C_D for the 3D square cylinder without and with SAC control at $Re = 22000$; (b) Temporal variations in smoothed C_L for the square cylinder without and with SAC control at $Re = 22000$; (c) and (d) are the power spectral density (PSD) of C_D and C_L respectively during the period of non-dimensional time ranging from 300 to 400. t^* represents non-dimensional time (one action step).

during the testing phase. This evaluation affords a detailed analysis of the agent performance across diverse flow conditions and facilitates a comparative study of their effectiveness in controlling the square cylinder flow field at high Re .

Fig. 8 (a) and (b) present the outcomes of the SAC algorithm. The entire training procedure occurs concurrently in 10 environments facilitated by DRLinFluids (Wang *et al.* 2022). The algorithm effectively learns to perform AFC, consistently diminishing drag and suppressing lift. In the baseline case, both C_D and C_L exhibit periodic oscillations around their mean values. Specifically, the mean value of C_D is 2.22, with standard deviations of 0.223 for C_D and 1.42 for C_L . With the DRL-based control, the mean value of C_D diminishes to 1.06, corresponding to a remarkable drag reduction of approximately 52.3%. Furthermore, the fluctuations in C_D and C_L experience significant suppression, with standard deviations reduced to 0.058 and 0.118, respectively. This represents a reduction of 74% and 91.7% compared to the baseline, respectively.

The power spectral density (PSD) analysis, comparing the behavior of C_D and C_L in cylinders with and without control, is presented in Fig. 8 (c) and (d). The C_L spectrum exhibits a peak at the dominant frequency $St = 1.3$, indicating distinct vortex shedding at this frequency, which contributes significantly to the energy responsible for both mean drag and fluctuations. In contrast, the PSD curves for C_D and C_L in the cylinder under SAC control show a disappearance of peaks, signifying the suppression of the regular vortex

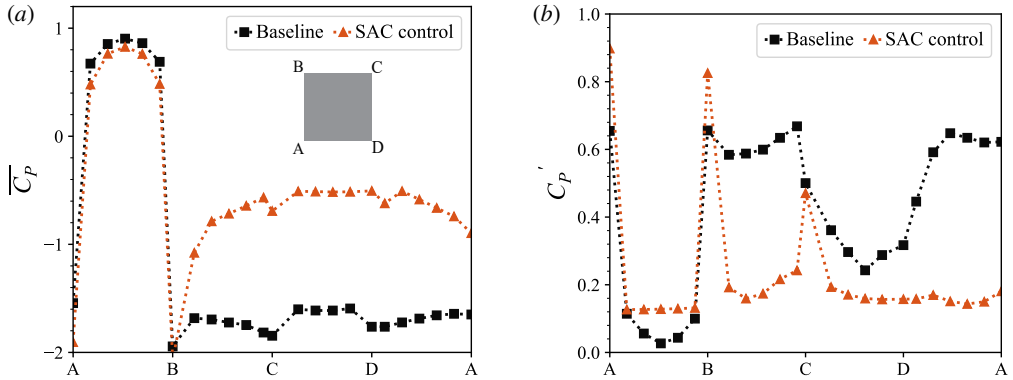


Figure 9: Mean and fluctuating pressure coefficient C_P distributions around the square cylinder for (a) the baseline case and (b) SAC control case.

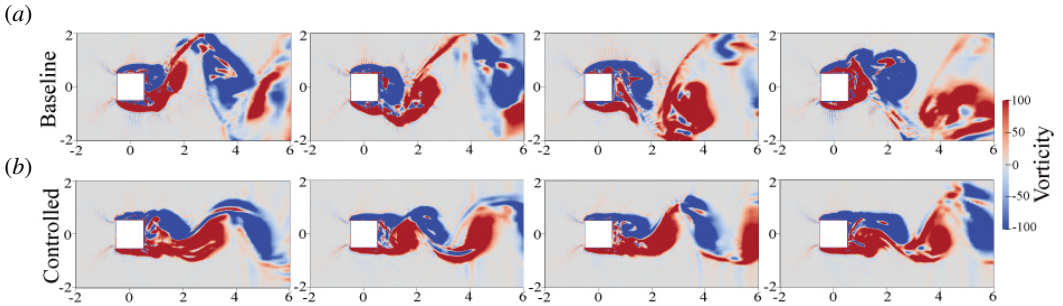


Figure 10: Instantaneous snapshots vorticity structures close to the surface of the square cylinder colored by the streamwise vorticity (a) without and (b) with SAC control

shedding pattern. Furthermore, the low-frequency regions of C_D and C_L are smaller than the baseline, aligning with the reduction in the fluctuations of C_D and C_L . This suggests that DRL-based control primarily diminishes drag and lift by suppressing energy in the relatively low-frequency range.

Fig. 9 shows the mean and fluctuating C_P on the surface of the square cylinder in both the baseline and the SAC control cases. The mean C_P exhibits minimal variation on the windward surface, suggesting that the jet flow has a negligible impact on the wind pressure in this region. However, notable differences emerge on the other three sides, particularly the leeward side. Besides, the negative C_P is significantly smaller in the control case compared to the baseline, leading to a reduction in C_D . The decrease in negative pressure on the leeward face enhances the overall pressure distribution, contributing to improved flow control and reduced drag on the square cylinder.

The fluctuations of C_P are depicted in Fig. 9 (b). On the windward side, the SAC control case exhibits a modest increasing in C_P fluctuations. Notably, on the leeward surface, the control case substantially suppresses C_P fluctuations compared to the baseline case, providing an explanation for the significant decrease in the standard deviation of C_L . It is noteworthy that the control case shows peaks in C_P fluctuations at the three corners of the square cylinder, attributable to vortex turbulence induced by the jet blowing and suction effect. However, these peaks do not compromise the overall reduction in C_P fluctuations, underscoring the effectiveness of the multiple jet configuration in controlling and minimizing C_P fluctuations.

Fig. 10 illustrates the instantaneous vorticity moments with and without control. In the uncontrolled flow field, small vortices tend to coil up, forming larger vortices that propagate

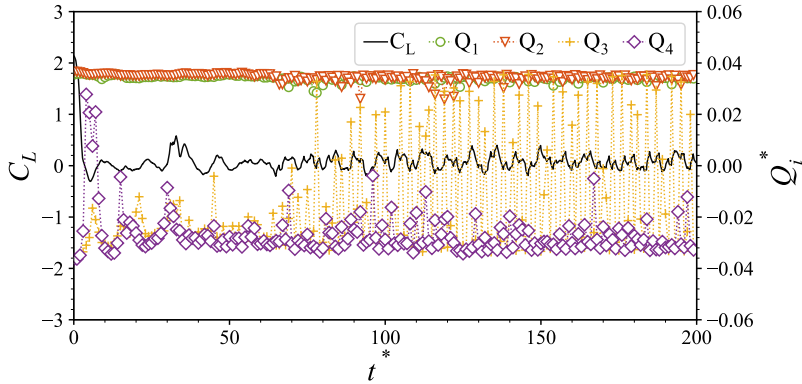


Figure 11: Time histories of C_L , and the mass flow rate corresponding to each jet actuator during SAC control period.

backward, resulting in an alternating shedding pattern. Notably, at the trailing edge of the square cylinder, the vortex channels exhibit increased length. The blowing and suction setup implements a control strategy utilizing the trailing-edge jet. This strategy efficiently utilizes the leading edge jets (Q_1 and Q_2) to disrupt the vortices, initially breaking down large vortices into smaller ones. Subsequently, the trailing edge jets (Q_3 and Q_4) are employed to push the smaller vortices away from the leeward wake region. This prevents the small vortices from attaching to the surface of the rectangular cylinder and forming large vortices, resulting in a more regular and synchronized shedding of vortices that is also more stable. The sequential attachment of small vortices to the surface of the square cylinder, forming a stable vortex channel along the flow direction, leads to the symmetrical shedding of vortices in the wake. As a result, the flow field formed by the shedding vortices follows a trajectory along the centerline symmetry, significantly reducing the drag and lift force of the square cylinder.

Furthermore, Fig. 11 illustrates C_L and jet actions of the DRL agent over a span of $200t^*$ for the control case. The blowing and suction mass flow rates exhibit varying patterns at the four corners of the square cylinder. Specifically, Q_1 and Q_2 consistently display inspiratory behavior, while Q_3 and Q_4 exhibit fluctuating states of blowing and suction. Examining the trend of C_L reveals a pseudo-periodic state emerging after $80t^*$. Notably, the fluctuation of Q_4 becomes more pronounced during this period, displaying alternating blowing and suction. This observation suggests that the fluctuating dynamics of blowing and suction at the trailing edge contribute to the stabilization of C_L . The fluctuation of C_L is effectively suppressed, underscoring the robustness of the strategy in stabilizing the vortex channel. This emphasizes the precision and effectiveness of the SAC control.

Considering the 3D vortex structure in the wake field, depicted in Figs. 12 (a) and (b), it becomes evident that in the absence of jet control, the wake region proximate to the square cylinder generates small and dispersed vortices. As the inlet flow progresses away from the cylinder, the small-scale vortex structures gradually dissipate, giving way to larger scale vortices. Conversely, when the DRL-based jet control is employed, a more regular and elongated vortex structure emerges. This result stems from the blowing and suction actions at the corners of the square cylinder, working in tandem with the inflowing airflow.

The elongated vortex structure which is reminiscent of the strip structure generated by the actuator, effectively mitigates the generation of fragmented vortices. Consequently, the mid and far wake regions exhibit a more orderly pattern characterized by alternating elongated vortices. Notably, the influence of leading edge blowing and suction is evident which can

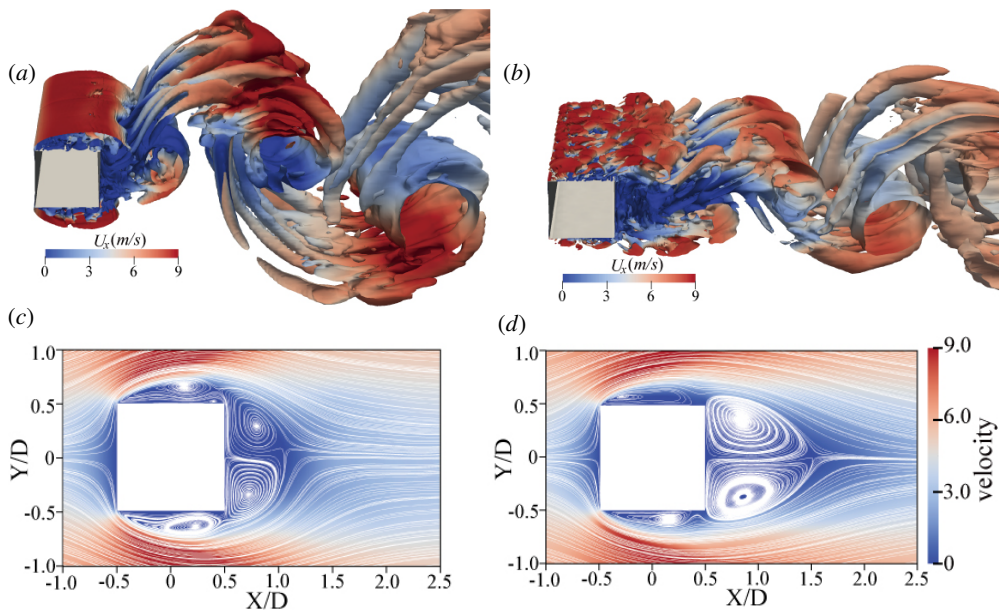


Figure 12: Turbulent flow past a square cylinder at $Re = 22000$. Instantaneous snapshots for iso-surfaces of Q-criterion colored by the streamwise velocity (a) without and (b) with SAC control, and streamlines of mean flow (c) without and (d) with SAC control.

transform large-scale flow braided vortices into predominantly smaller and finely fragmented vortices. Concurrently, trailing edge blowing and suction displace these small vortices, forming a narrower wake, indicative of reduced drag. The integration of a DRL-based jet actuator introduces controlled airflow that significantly shapes wake characteristics. The resulting elongated vortex structure exhibits enhanced regularity and coherence, pointing towards improved airflow control. These controlled vortex structures hold the potential to enhance aerodynamic performance, minimize drag, or achieve other desired flow control objectives across diverse engineering applications.

The width and length of the wake recirculation zone exert a direct influence on the base pressure behind the square cylinder. Illustrated in Fig. 12 (c) and (d), the wake region of the cylinder subject to DRL-based actuation exhibits (1) a constriction of the secondary vortex, (2) an 11.8% reduction in the maximum width of the wake stream, and (3) an elongation of the wake stream length by 80% compared to the uncontrolled cylinder. These three factors collectively contribute to a significant decrease in drag, and the constriction of the secondary vortex mitigates the adverse impact on C_L . This holistic effect results in a pronounced drag reduction of approximately 52.3%.

To comprehend the blow-suction controller mechanism, proper orthogonal decomposition (POD) analyses are conducted based on fluctuating kinetic energy for both baseline and controlled flows to delineate distinctions in their unsteady flow structures. Fig. 13 illustrates the streamwise velocity components for the baseline and SAC controlled flows, focusing on the first three POD modes. In the unforced flow, vortices initiate development at the leading edge of the square cylinder, culminating in the formation of a large vortex at the trailing edge and exhibiting a symmetric distribution. After control, it becomes evident that the vortex undergoes suction at the leading edge of the square cylinder, corresponding to the actions of Q_1 and Q_2 depicted in Fig. 11. Consequently, the vortex no longer coils into a large structure on the surface of the square cylinder. Moreover, the blowing and suction actions of

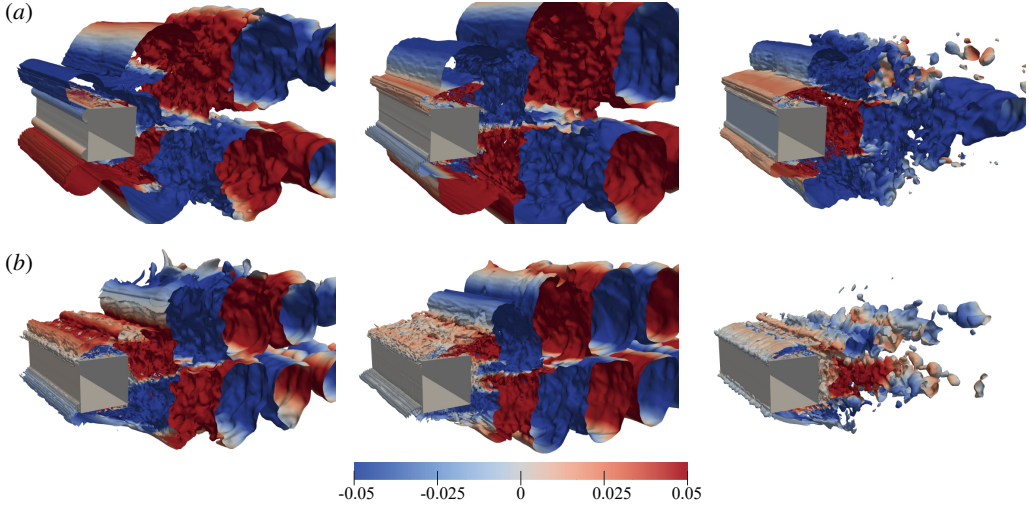


Figure 13: Streamwise velocity components of the first three POD modes for: (a) baseline flow, (b) flow with the SAC control.

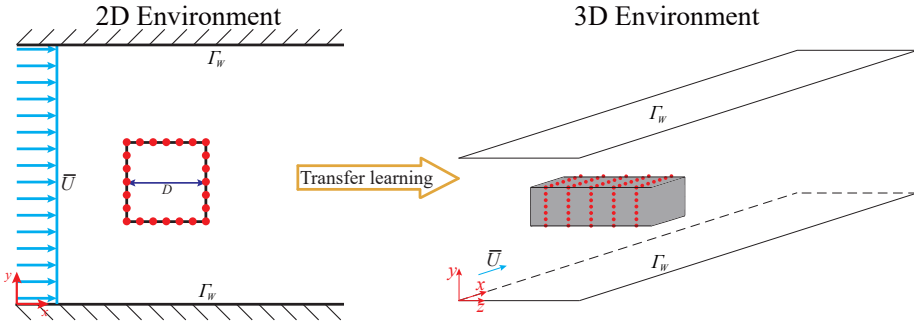


Figure 14: Process of transfer learning under state dimension mismatch from 2D square cylinder flow field to 3D square cylinder environments.

Q_3 and Q_4 at the trailing edge push the vortex away, expanding the recirculation zone in the wake region of the square cylinder. Consequently, the symmetric vortex size across the three modes is diminished compared to the unforced flow. In conclusion, the DRL jet blowing and suction actuator postpones the formation of major vortices, thereby further mitigating pressure fluctuations induced by these vortices in the square cylinder.

4.2. Flow control results using the SDTL-SAC algorithm

As depicted in Fig. 14, in order to facilitate transfer learning from a 2D flow field to a 3D flow field, 24 pressure probes are uniformly deployed on the surface of the 2D square cylinder flow field. Additionally, 24 pressure probes in each of the five circles are arranged to comprehensively explore the flow field information in the 3D flow field. In both square cylinder cases, flow control is achieved through four jets located at the corners of the square cylinder. The objective of SDTL-SAC is to expedite the convergence of transfer learning in the presence of state space mismatch problems.

Control results of this blowing and suction configuration in 2D square cylinder flow field as illustrated in Fig. 15, extensive DRL training of the blowing and suction configuration

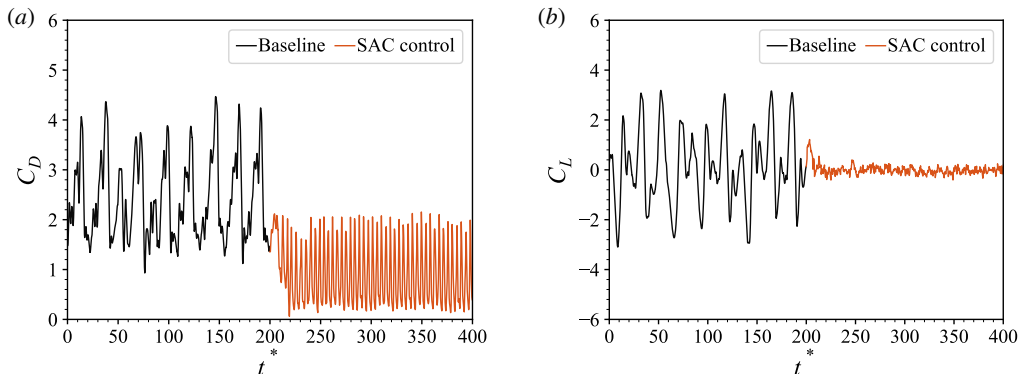


Figure 15: (a) Evolution of C_D for the 2D square cylinder without (no jet) and with SAC control at $Re = 1000$; (b) Temporal variations in smoothed C_L for the square cylinder without (no jet) and with SAC control at $Re = 1000$.

resulted in significant drag and lift reduction performance at the condition of 2D flow field and $Re = 1000$. Specifically, the drag reduction ratio reached 63.2%, accompanied by a reduction of 30.3% in drag fluctuation and an impressive 93.1% reduction in lift fluctuation. These outcomes underscore the efficacy of the four jets blowing and suction policy, particularly in the flow field of the 2D square cylinder. This control performance lays the foundation for transfer policy to a 3D flow field of the square cylinder.

Fig. 16(a) illustrates the variation in mean C_D with an increasing number of DRL training sets, comparing the training conditions of basic SAC and SDTL-SAC algorithms. Both algorithms undergo parallel training in 10 environments (Wang *et al.* 2023b), demonstrating substantial drag reduction compared to the baseline. Specifically, compared with the baseline, the mean C_D of the two algorithms SAC and SDTL-SAC is reduced to 1.06 and 1.03 respectively. Another contributing factor to the difference in reward value growth rate is the standard deviation of C_L , as depicted in Fig. 16(b). While the SAC algorithm reduces lift fluctuation to 0.20, the SDTL-SAC method promptly suppresses square cylinder lift fluctuation, reaching 0.13 by episode 90. The SDTL-SAC method exhibits the ability to attain a superior control level within a shorter timeframe when confronted with state dimension mismatch during transfer learning.

However, notable distinctions emerge from the reward learning curve presented in Fig. 16(c). The reward curve of the SDTL-SAC method shows a faster upward trend throughout the process, eventually reaching around -106. In contrast, the SAC algorithm encounters instability between episodes 50 and 180, marked by significant fluctuations followed by a relatively low value after training completion. Additionally, the reward curve can serve as a criterion for assessing the convergence of DRL training. It is evident that the SDTL-SAC method significantly accelerates DRL training progress. Specifically, basic SAC training from scratch requires 160 episodes to achieve convergence, while training a 2D square cylinder pre-trained policy with SDTL-SAC method only requires approximately 70 epochs to do so.

Fig. 16(d) illustrates the computational resources efficiency of the SDTL-SAC method. The basic SAC training demands substantial computational time and resources. In the case of computational resource consumption of the SDTL-SAC method, the training of the 2D control policy accounts for only 3.3% of the total computational resources. The transfer retaining phase, meaning transfer learning in the 3D flow field with the pre-trained model, occupies 45.6% of the total computational resources. In addition, the SDTL-SAC method achieves a noteworthy reduction in computational time, reducing 51.1% of the original training time.

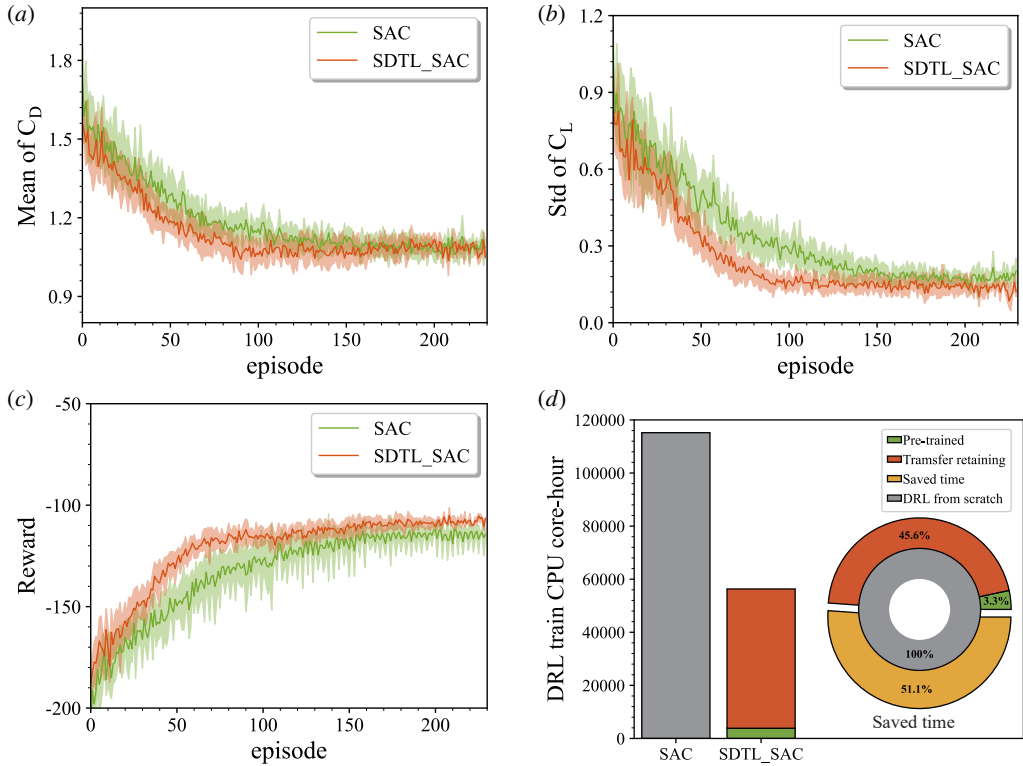


Figure 16: Evolution of (a) mean drag reduction, (b) reward, and (c) std of lift coefficient with basic SAC and SDTL-SAC method, respectively; (d) shows the computational resources saved by SDTL-SAC method.

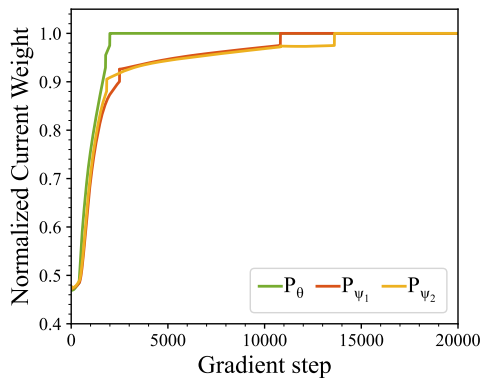


Figure 17: The value of the weighting assigned to the current policy representations, denoted as p_θ , p_{ψ_1} , p_{ψ_2} , within the context of the weighted linear combination is explored during the transfer process of a 2D square cylinder control policy to 3D square cylinder environments.

This highlights the significant time savings afforded by the SDTL-SAC method in DRL training, even under state dimensions mismatch.

As illustrated in Fig. 17, the learnable mixing weights p_θ , p_{ψ_1} , p_{ψ_2} undergo evolution over time. As the training process advances, these weights progressively converge toward 1. In

the initial stages of training, the current policy gradually assimilates valuable representations from the source policy until achieving complete independence from the source policy. In addition, the success of cross-domain transfer learning hinges on the task similarity between the current and source policy.

5. Conclusions and outlook

This study represents a notable advancement in practical AFC by utilizing a surface pressure sensor situated on a square cylinder as the sole input to the DRL agent. The study focuses on transfer learning from 2D to 3D square cylinder flow fields in the state dimensional mismatch by employing the proposed SDTL-SAC method, resulting in significant acceleration outcomes. This method holds promising implications for enhancing DRL applications in real-world scenarios, particularly in the reduction of drag and lift forces for structures like high-rise buildings. The primary findings of this study are succinctly outlined as follows.

First, the basic SAC algorithm is arranged to numerically simulate active control of a 3D square cylinder at $Re = 22000$. The utilization of the DRL algorithm specifically with multiple jets control, led to a substantial reduction in C_D reaching an impressive 52.3%. Concurrently, fluctuations in both C_D and C_L are suppressed by 74% and 91.7%, respectively. During the last phase of the control process, the agent maintained a significant action amplitude, effectively disrupting the vortices on both sides of the square cylinder. Consequently, the vortices adhered to the square cylinder surface and experienced delayed shedding, contributing to a reduction in lift impact generated by the square cylinder. This precise adaptive control strategy demonstrated superior flow control performance for the jet configuration. Additionally, the mean velocity contours illustrated that the blowing and suction multiple jets have the potential to effectively manipulate vortex shedding patterns in the flow field of square cylinders. The effectiveness of this approach in enhancing aerodynamic performance is underscored.

Furthermore, the training speed of DRL is enhanced while preserving performance by introducing the State dimensional transfer Learning with the soft actor-critic algorithm (SDTL-SAC). This transfer learning algorithm accommodates situations where the current and source agents possess arbitrarily different state dimension. The key innovation involves training an encoder to generate embeddings and extracting valuable representations from the source network. Experiments on a transfer task from 2D to 3D square cylinder flow field, demonstrate that the SDTL-SAC algorithm accelerates the training process for high Re square cylinders which can lead to up to a 51.1% reduction in training time. Additionally, the results indicate that transfer learning contributes to more stable decision-making, potentially enhancing its utility in flow control applications.

Transfer learning is a widely explored research domain, and the judicious selection of transfer learning methods tailored to specific fluid dynamic systems can significantly enhance control efficiency within a reduced timeframe. Leveraging these features and incorporating them as states in DRL holds considerable promise. A natural progression of this methodology involves extending its application to accommodate transfer learning across distinct state and action spaces, introducing a more realistic yet inherently complex implementation challenge. The SDTL-SAC method emerges as a robust approach for transfer learning across diverse flow fields, yielding optimal reductions in C_D and C_L at elevated Reynolds numbers. This method holds the potential for effectively managing intricate fluid dynamic systems. By integrating existing research on 2D and 3D flow control with transfer learning, we aim to enhance the understanding of the behavior of real flow fields and pave the way for more effective implementation of flow field control. The significance of this study lies in its contribution

Table 2: Configurations of flow simulation

Parameter	Value
Flow simulation set-up	
Numerical time step (non-dimensional dt)	5×10^{-5}
Maximum action amplitude (non-dimensional)	3
Control step length	$100 dt$
SAC hyperparameters	
Actor architecture	512×256 (two fully connected layers)
Critic architecture	512×256 (two fully connected layers)
Actor leaning rate	3×10^{-4}
Critic leaning rate	2×10^{-4}
Discount factor	0.97
Alpha	0.5
Optimiser	Adam(Kingma <i>et al.</i> 2015)
SDTL-SAC hyperparameters	
Parallelized environments	10
Number of action per episode	80 (Wang <i>et al.</i> 2022)
CPU time per episode	2.5h

to advancing the field of flow control, offering more reliable and efficient solutions for engineering applications and scientific research.

Acknowledgement

This study is supported by National Natural Science Foundation of China (52278493, 52108451), Shenzhen Science and Technology Program (KQTD20210811090112003). This work is also supported by National Science Foundation of China (NSFC) through grants 12172109 and 12172111.

Appendix A. Hyperparameters

Table 2 presents the main numerical parameters of both the simulated case and the learning algorithm.

Appendix B. State dimension mismatch transfer learning.

Algorithm 1 describes the steps of SDTL-SAC.

REFERENCES

- BARTON, IAIN EDWARD 1998 Comparison of simple-and piso-type algorithms for transient flows. *International Journal for numerical methods in fluids* **26** (4), 459–483.
- CHEN, WENJIE, WANG, QIULEI, YAN, LEI, HU, GANG & NOACK, BERND R 2023 Deep reinforcement learning-based active flow control of vortex-induced vibration of a square cylinder. *Deep reinforcement learning-based active flow control of vortex-induced vibration of a square cylinder. Physics of Fluids* **35** (5).
- FAN, DIXIA, YANG, LIU, WANG, ZHICHENG, TRIANTAFYLLOU, MICHAEL S & KARNIADAKIS, GEORGE EM 2020 Reinforcement learning for bluff body active flow control in experiments and simulations. *Proceedings of the National Academy of Sciences* **117** (42), 26091–26098.

Algorithm 1: SDTL algorithm with Soft Actor-Critic.

Input: θ', ψ'_i : fixed source policy and value networks θ', ψ'_i
 θ, ψ_i : current policy and value networks
 ϕ_π, ϕ_i : policy and value state encoder parameters
 ω_π, ω_i : policy and value variational distribution parameters
 $\{p_\pi\}, \{p_i\}$: set of coupling parameters for policy and value networks
Initialization: target network weights $\bar{\theta}_i \leftarrow \theta_i$, replay buffer $\mathcal{D} \leftarrow \emptyset$
for each iteration do
 for each environment step do
 $a_t \sim \pi_\phi(a_t | s_t)$;
 $s_{t+1} \sim p(s_{t+1} | s_t, a_t)$;
 $\mathcal{S}_t \leftarrow \mathbf{g}(\{s_1, s_2, \dots, s_{t+1}\} \cup \{a_1, a_2, \dots, a_t\})$;
 $\mathcal{D} \leftarrow \mathcal{D} \cup \{(\mathcal{S}_t, a_t, r(s_t, a_t))\}$;
 end
 for each gradient step do
 Update ψ_i with $\lambda_Q \hat{\nabla}_{\psi_i} L_Q(\psi_i, \phi_i, \psi'_i)$ for $i \in 1, 2$;
 Update ϕ_i with $\hat{\nabla}_{\phi_i} [L_Q(\psi_i, \phi_i, \psi'_i) + L_{\text{MI}}^Q(\phi_i, \omega_i)]$ for $i \in 1, 2$;
 Update ω_i with $\hat{\nabla}_{\omega_i} L_{\text{MI}}^Q(\phi_i, \omega_i)$ for $i \in 1, 2$;
 Update $\{p_\psi\}$ using $[L_{\text{coupling}}^Q + L_Q]$
 Update θ with $\lambda_\pi \hat{\nabla}_\theta L_\pi(\theta, \phi_\pi, \theta')$;
 Update ϕ_π with $\hat{\nabla}_{\phi_\pi} [L_\pi(\theta, \phi_\pi, \theta') + L_{\text{MI}}^\pi(\phi_\pi, \omega_\pi)]$;
 Update ω_π with $\hat{\nabla}_{\omega_\pi} L_{\text{MI}}^\pi(\phi_\pi, \omega_\pi)$;
 Update $\{p_\pi\}$ using $[L_{\text{coupling}}^\pi + L_\pi]$
 Update $\bar{\theta}_i$ and α according to (Haarnoja *et al.* 2018);
 end
end

- GAZZOLA, MATTIA, TCHIEU, ANDREW A, ALEXEEV, DMITRY, DE BRAUER, ALEXIA & KOUMOUTSAKOS, PETROS 2016 Learning to school in the presence of hydrodynamic interactions. *Journal of Fluid Mechanics* **789**, 726–749.
- GUASTONI, LUCA, RABAULT, JEAN, SCHLATTER, PHILIPP, AZIZPOUR, HOSSEIN & VINUESA, RICARDO 2023 Deep reinforcement learning for turbulent drag reduction in channel flows. *Eur. J. Phys., To Appear*. Preprint arXiv:2301.09889 .
- HAARNOJA, TUOMAS, ZHOU, AURICK, ABBEEL, PIETER & LEVINE, SERGEY 2018 Soft actor-critic: Off-policy maximum entropy deep reinforcement learning with a stochastic actor. In *International conference on machine learning*, pp. 1861–1870. PMLR.
- HAN, BING-ZHENG, HUANG, WEI-XI & XU, CHUN-XIAO 2022 Deep reinforcement learning for active control of flow over a circular cylinder with rotational oscillations. *International Journal of Heat and Fluid Flow* **96**, 109008.
- HE, XIAN-JUN, WANG, YI-ZHE, HUA, YUE, CHEN, ZHI-HUA, LI, YU-BAI & WU, WEI-TAO 2023 Policy transfer of reinforcement learning-based flow control: From two-to three-dimensional environment. *Physics of Fluids* **35** (5).
- JASAK, HRVOJE, JEMCOV, ALEKSANDAR & TUKOVIC, ZELJKO 2007 Openfoam: A c++ library for complex physics simulations. In *International workshop on coupled methods in numerical dynamics*, , vol. 1000, p. 1–20. IUC Dubrovnik Croatia.
- KINGMA, DIEDERIK P, BA, JIMMY, BENGIO, Y & LECUN, Y 2015 3rd international conference on learning representations. *ICLR, San Diego* .
- LI, SHAO-PENG, SNAIKI, REDA & WU, TENG 2021 A knowledge-enhanced deep reinforcement learning-based

- shape optimizer for aerodynamic mitigation of wind-sensitive structures. *Computer-Aided Civil and Infrastructure Engineering* **36** (6), 733–746.
- LILLICRAP, TIMOTHY P, HUNT, JONATHAN J, PRITZEL, ALEXANDER, HEESS, NICOLAS, EREZ, TOM, TASSA, YUVAL, SILVER, DAVID & WIERSTRA, DAAN 2015 Continuous control with deep reinforcement learning. *arXiv preprint arXiv:1509.02971* .
- LIU, RUO-LIN, HUA, YUE, ZHOU, ZHI-FU, LI, YUBAI, WU, WEI-TAO & AUBRY, NADINE 2022 Prediction and optimization of airfoil aerodynamic performance using deep neural network coupled bayesian method. *Physics of Fluids* **34** (11).
- NICOUD, FRANCK & DUCROS, FRÉDÉRIC 1999 Subgrid-scale stress modelling based on the square of the velocity gradient tensor. *Flow, turbulence and Combustion* **62** (3), 183–200.
- PARIS, ROMAIN, BENEDDINE, SAMIR & DANDOIS, JULIEN 2021 Robust flow control and optimal sensor placement using deep reinforcement learning. *Journal of Fluid Mechanics* **913**.
- PARIS, ROMAIN, BENEDDINE, SAMIR & DANDOIS, JULIEN 2023 Reinforcement-learning-based actuator selection method for active flow control. *Journal of Fluid Mechanics* **955**, A8.
- RABAULT, JEAN, KUCHTA, MIROSLAV, JENSEN, ATLE, RÉGLADE, ULYSSE & CERARDI, NICOLAS 2019 Artificial neural networks trained through deep reinforcement learning discover control strategies for active flow control. *Journal of Fluid Mechanics* **865**, 281–302.
- REN, FENG, WANG, CHENGLI & TANG, HUI 2019 Active control of vortex-induced vibration of a circular cylinder using machine learning. *Physics of Fluids* **31** (9), 093601.
- REN, FENG, WANG, CHENGLI & TANG, HUI 2021 Bluff body uses deep-reinforcement-learning trained active flow control to achieve hydrodynamic stealth. *Physics of Fluids* **33** (9), 093602.
- RODI, WOLFGANG, FERZIGER, JOEL H, BREUER, MICHAEL, POURQUIÉ, MATHIEU & OTHERS 1997 Status of large eddy simulation: results of a workshop. *Transactions-American Society of Mechanical Engineers Journal of Fluids Engineering* **119**, 248–262.
- SAEEDI, MOHAMMAD & WANG, BING-CHEN 2016 Large-eddy simulation of turbulent flow around a finite-height wall-mounted square cylinder within a thin boundary layer. *Flow, Turbulence and Combustion* **97**, 513–538.
- SUÁREZ, POL, ALCÁNTARA-ÁVILA, FRANCISCO, MIRÓ, ARNAU, RABAULT, JEAN, FONT, BERNAT, LEHMKUHL, ORIOL & VINUESA, R 2023 Active flow control for three-dimensional cylinders through deep reinforcement learning. *arXiv preprint arXiv:2309.02462* .
- TANG, HONGWEI, RABAULT, JEAN, KUHNLE, ALEXANDER, WANG, YAN & WANG, TONGGUANG 2020 Robust active flow control over a range of reynolds numbers using an artificial neural network trained through deep reinforcement learning. *Physics of Fluids* **32** (5), 053605.
- TRIAS, F XAVIER, GOROBETS, ANDREI & OLIVA, A 2015 Turbulent flow around a square cylinder at reynolds number 22,000: A dns study. *Computers & Fluids* **123**, 87–98.
- VIGNON, COLIN, RABAULT, JEAN & VINUESA, RICARDO 2023 Recent advances in applying deep reinforcement learning for flow control: Perspectives and future directions. *Physics of Fluids* **35** (3).
- VIQUERAT, JONATHAN, RABAULT, JEAN, KUHNLE, ALEXANDER, GHRAIEB, HASSAN, LARCHER, AURÉLIEN & HACHEM, ELIE 2021 Direct shape optimization through deep reinforcement learning. *Journal of Computational Physics* **428**, 110080.
- VOKE, PETER R 1997 Flow past a square cylinder: test case les2. In *Direct and Large-Eddy Simulation II: Proceedings of the ERCOFTAC Workshop held in Grenoble, France, 16–19 September 1996*, pp. 355–373. Springer.
- WAN, MICHAEL, GANGWANI, TANMAY & PENG, JIAN 2020 Mutual information based knowledge transfer under state-action dimension mismatch. *arXiv preprint arXiv:2006.07041* .
- WANG, QIULEI, YAN, LEI, HU, GANG, CHEN, WENLI, RABAULT, JEAN & NOACK, BERND R 2023a Dynamic feature-based deep reinforcement learning for flow control of circular cylinder with sparse surface pressure sensing. *arXiv preprint arXiv:2307.01995* .
- WANG, QIULEI, YAN, LEI, HU, GANG, LI, CHAO, XIAO, YIQING, XIONG, HAO, RABAULT, JEAN & NOACK, BERND R 2022 Drlinfluids: An open-source python platform of coupling deep reinforcement learning and openfoam. *Physics of Fluids* **34** (8), 081801.
- WANG, ZHICHENG, FAN, DIXIA, JIANG, XIAOMO, TRIANTAFYLLOU, MICHAEL S & KARNIADAKIS, GEORGE EM 2023b Deep reinforcement transfer learning of active control for bluff body flows at high reynolds number. *Journal of Fluid Mechanics* **973**, A32.
- YAN, LEI, LI, YUERONG, HU, GANG, CHEN, WEN-LI, ZHONG, WEI & NOACK, BERND R 2023 Stabilizing the square cylinder wake using deep reinforcement learning for different jet locations. *Physics of Fluids* **35** (11).

- YANG, ZHIYIN 2015 Large-eddy simulation: Past, present and the future. *Chinese journal of Aeronautics* **28** (1), 11–24.
- YOU, HENG, YANG, TIANPEI, ZHENG, YAN, HAO, JIANYE & E TAYLOR, MATTHEW 2022 Cross-domain adaptive transfer reinforcement learning based on state-action correspondence. In *Uncertainty in Artificial Intelligence*, pp. 2299–2309. PMLR.
- ZHENG, CHANGDONG, JI, TINGWEI, XIE, FANGFANG, ZHANG, XINSHUAI, ZHENG, HONGYU & ZHENG, YAO 2021 From active learning to deep reinforcement learning: Intelligent active flow control in suppressing vortex-induced vibration. *Physics of Fluids* **33** (6), 063607.